Materials Advances

ROYAL SOCIETY OF CHEMISTRY

PAPER

View Article Online
View Journal | View Issue

Check for updates

Cite this: *Mater. Adv.*, 2022, 3, 7569

A sensitive fluorescent sensor based on terpyridine@Zn^{2+}-modified mesoporous silica for the detection of sulfonamide antibiotics†

Qian Zhao and Jing Wang *

The sensitive detection of sulfonamide antibiotic (SA) residues is of great significance to ecosystems and public health. To overcome the defect of poor water dispersion stability and low sensitivity of SA detection systems, a terpyridine@Zn^{2+}-modified mesoporous silica, denoted ATpy@Zn-SBA-15, was developed and applied as a highly sensitive and quickly responsive fluorescent sensor for the detection of SAs in tap water and milk. Terpyridine, with three pyridine groups, can form a stable complex with Zn^{2+}. The Zn^{2+} in terpyridine@Zn^{2+} provides binding sites to recognize SAs such as sulfathiazole (STZ) by forming conjugates between ATpy@Zn-SBA-15 and STZ, thus facilitating energy transfer from the organic functional groups of ATpy@Zn-SBA-15 to STZ, resulting in efficient changes in fluorescence spectra. When the concentration of SAs such as STZ increased, the fluorescence emission intensity of ATpy@Zn-SBA-15 suspensions at 429 nm gradually decreased. ATpy@Zn-SBA-15 exhibited relatively low detection limits of 0.17, 0.63, 0.52, 0.57 and 0.54 μM for STZ, sulfamethizole, sulfachlorpyridazine, sulfamerazine and sulfamethoxypyridazine, respectively. Compared with the material without Zn^{2+}, ATpy@Zn-SBA-15 displayed remarkably enhanced SA sensitivity, which demonstrated that introducing the Zn^{2+} sites played a crucial role for both specific recognition of SAs and fluorescence response signals. Prominently, this proposed strategy can be applied for detecting other antibiotics by varying the organic functional groups and metal sites.

Received 5th May 2022,
Accepted 28th July 2022

DOI: 10.1039/d2ma00504b

rsc.li/materials-advances

Open Access Article. Published on 30 July 2022. Downloaded on 2/8/2026 2:57:13 PM.
This article is licensed under a Creative Commons Attribution-NonCommercial 3.0 Unported Licence.

1. Introduction

Currently, China is both the largest producer and consumer of antibiotics in the world.[1] The widespread use of antibiotics has attracted public attention due to its potential threat to the environment and human health.[2,3] Among these antibiotics, sulfonamide antibiotics (SAs) such as sulfathiazole (STZ), sulfamethizole (SMT), sulfachlorpyridazine (SCP), sulfamerazine (SMR) and sulfamethoxypyridazine (SMP) are found in many aquatic environments, soils, and sediments worldwide.[1,4–10] Due to the high toxicity and stability of SAs in the environment, an increasing number of concerns have been raised. A variety of methods such as capillary electrophoresis, high-performance liquid chromatography (HPLC), gas chromatography-mass spectrometry (GC-MS) and HPLC-MS are widely used in the field of SA detection.[11–14] However, most existing methods appear to be either too expensive or too time-consuming and tedious. Thus, it is urgent to develop a simpler, more effective, economical and rapid method for the determination of trace SAs in aqueous medium.

The fluorescent sensing method remains attractive due to its high sensitivity, simple operation procedures and rapid response.[15] In this context, organic–inorganic hybrids such as metal–organic framework,[15] quantum dots,[16] and molecularly imprinted polymer,[17] present more attractive properties than organic-based fluorescent detection systems, due to the combined advantages of inorganic and organic functions.[18,19] Although some progress has been made, most of the antibiotic fluorescent sensors may need cumbersome preparation procedures, lack pH and water dispersion stability, and display low sensitivity and anti-interference abilities.[20,21] For example, a few recent reports included the detection of residual antibiotics performed in organic solvents, such as methanol (MeOH),[22] *N*,*N*-dimethylformamide,[23] and *N*,*N*-dimethylacetamide,[24] *etc.*, due to the lack of water dispersibility or water stability. Moreover, the concentration of SA residues in water and some foods like milk is extremely low, requiring detection systems with high sensitivity, which is of great significance. Therefore, great efforts are still required to improve the water dispersion stability and sensitivity of the organic–inorganic hybrids in order to put the application into practical detection.

School of Chemistry and Chemical Engineering, Guangxi University, Nanning 530004, P. R. China. E-mail: wjwyj82@gxu.edu.cn

† Electronic supplementary information (ESI) available. See DOI: https://doi.org/10.1039/d2ma00504b

© 2022 The Author(s). Published by the Royal Society of Chemistry

Open Access Article. Published on 30 July 2022. Downloaded on 2/8/2026 2:57:13 PM.
This article is licensed under a Creative Commons Attribution-NonCommercial 3.0 Unported Licence.

To overcome the defect of poor water dispersibility or stability of the detection systems, mesoporous silica materials, such as SBA-15, have been adopted as excellent solid support matrix for organic functional groups, taking advantage of their outstanding hydrothermal stability, sufficient mechanical resistance, high surface area and easy functionalization of properties.[15,20,21,25] Functionalized mesoporous silica materials have been extensively developed in sensing applications,[18] whereas the application of organic-embedded mesoporous silica materials is limited to detecting trace amounts of antibiotics. In general, functionalized mesoporous silica materials have been constructed as fluorescent sensors by immobilizing the fluorescent signaling unit and target recognition unit into the mesoporous silica matrix.[26–29] Thus, the functionalization of mesoporous silica with SA-responsive units is particularly important for improving SA sensitivity. It is noteworthy that the molecular structure of SAs contains heteroatoms such as nitrogen, oxygen and sulfur, which can provide lone-pair electrons to coordinate with metal ions and form stable complexes,[30,31] providing a theoretical basis for the application of metal-containing systems in the detection of SAs. Currently, metal-doped nanomaterials have been developed and widely applied to solve environmental problems,[32–35] while the integration of SA-coordinated metal ions with functionalized mesoporous silica has not been well explored. Therefore, the functionalization of mesoporous silica with SA binding sites could be particularly interesting and is expected to become an ideal design strategy for SA detection.

With these above considerations in mind, herein, an organic–metal complex of CTpy@Zn^{2+} was initially synthesized by coordinating the electron-rich 4-chloro-2, 2′ : 6′,2″-terpyridine (CTpy) and Zn^{2+}, and then CTpy@Zn^{2+} was embedded into the mesoporous SBA-15 silica, generating ATpy@Zn-SBA-15 as a fluorescent sensor for the sensitive detection of SAs in tap water and milk. In the detection of SAs, the fluorescence of ATpy@Zn-SBA-15 was efficiently quenched, with CTpy@Zn^{2+} acting as both recognition and fluorescence signaling unit. Furthermore, the detection mechanism has been studied according to the experimental results and theoretical calculations.

2. Experimental

2.1. Materials and instruments

SBA-15 was purchased from Nanjing XFNANO Materials Tech Co. Ltd (China). (3-Aminopropyl)triethoxysilane (APTES) was purchased from Sigma-Aldrich; CTpy and (2-hydroxyethyl)-1-piperazineethanesulfonic acid (HEPES) were purchased from Shanghai Aladdin Biochemical Technology Co. Ltd (China). All other reagents were obtained from commercial suppliers and used as received unless otherwise noted.

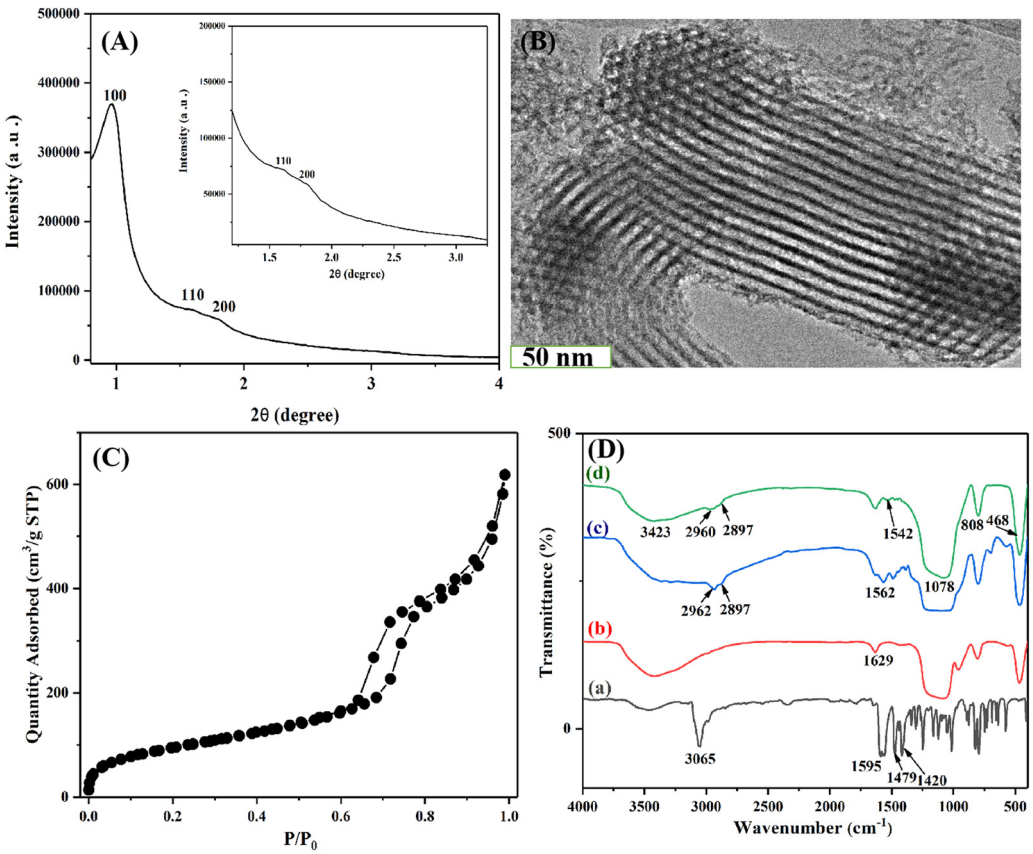

Fig. 1 (A) SXRD pattern, (B) TEM image and (C) N_2 adsorption–desorption isotherms of ATpy@Zn-SBA-15. (D) FT-IR spectra of (a) CTpy@Zn^{2+}, (b) SBA-15, (c) APTES-SBA-15, and (d) ATpy@Zn-SBA-15.

© 2022 The Author(s). Published by the Royal Society of Chemistry

Open Access Article. Published on 30 July 2022. Downloaded on 2/8/2026 2:57:13 PM.
This article is licensed under a Creative Commons Attribution-NonCommercial 3.0 Unported Licence.

The characterization methods used herein include Fourier transform infrared spectroscopy (FT-IR; Therm Nicolet iS50), small-angle X-ray diffractometry (SXRD; Brucker D8), transmission electron microscopy (TEM; JEM-2800), nitrogen adsorption–desorption isotherms (TriStar II 3020), and thermogravimetric analysis (TGA; STA2500); ^{13}C and ^{29}Si CP magic-angle spinning (MAS) NMR spectra were obtained on a Bruker AVANCE III HD 600 MHZ spectrometer at a ^{29}Si resonance frequency of 119.23 MHz and a ^{13}C resonance frequency of 150.92 MHz. Fluorescence spectra were detected on a 960 MC spectroscope (Shanghai Lengguang Technology Co. Ltd, China), with an excitation wavelength of 298 nm. The UV-Vis spectra were detected on a UV 1901 spectroscope. The fluorescence lifetimes were recorded using FL3C-111 TCSPC. The pH was measured by a Mettler Toledo S20K pH meter.

2.2. Preparation of ATpy@Zn-SBA-15

2.2.1. Synthesis of CTpy@Zn^{2+}. As shown in Scheme 1, $ZnCl_2$ (0.0844 g, 0.6 mmol) was ultrasonically dispersed in 5 mL anhydrous ethanol; CTpy (0.1317 g, 0.5 mmol) in 5 mL chloroform was then added drop by drop. The reaction mixture was stirred for 12 h at room temperature. The precipitate was collected by filtration, washed with anhydrous ethanol (5 × 20 mL), and dried at 80 °C for 12 h. Subsequently, white solid CTpy@Zn^{2+} was obtained (0.1806 g, 0.45 mmol, 90.87% yield). Characterization of CTpy@Zn^{2+}: FT-IR spectra (KBr, ν, cm^{-1}, Fig. 1D): 3065, 1595, 1479 and 1420 cm^{-1}.

2.2.2. Preparation of ATpy@Zn-SBA-15. The preparation method for APTES-SBA-15 was recently reported in our previous work.[36] About 0.1 g of APTES-SBA-15 was ultrasonically dispersed in 30 mL anhydrous ethanol and stirred at 80 °C for 20 min, and about 0.05 g of CTpy@Zn^{2+} was then added. The reaction mixture was stirred under reflux for 24 h. The final product was isolated by centrifugation and washed with water (5 × 20 mL) to remove unreacted CTpy@Zn^{2+}. ATpy@Zn-SBA-15 was collected as a pale pink powder and dried at 80 °C for 12 h (Scheme 1).

2.3. Preparation of CTY@SBA

About 0.05 g of APTES-SBA-15 was ultrasonically dispersed in 30 mL $CHCl_3$ and stirred at 62 °C for 20 min, and about 0.05 g of CTpy was then added. The reaction mixture was stirred under reflux for 24 h. The final product was isolated by centrifugation and washed with $CHCl_3$ (5 × 20 mL) to remove unreacted CTpy. CTY@SBA was collected as a white powder and dried at 80 °C for 12 h (Scheme 1).

2.4. Preparation of antibiotic stock solutions

All stock solutions were prepared according to a typical process. Taking STZ for example, 22.6 mg of STZ (0.089 mmol) was added to 200 μL solution of NaOH (0.1 M) and dissolved under ultrasound. Deionized water was then added to a constant volume of 22 mL, and the resulting solution was used as a stock solution (4×10^{-3} M, pH ≈ 7.0).

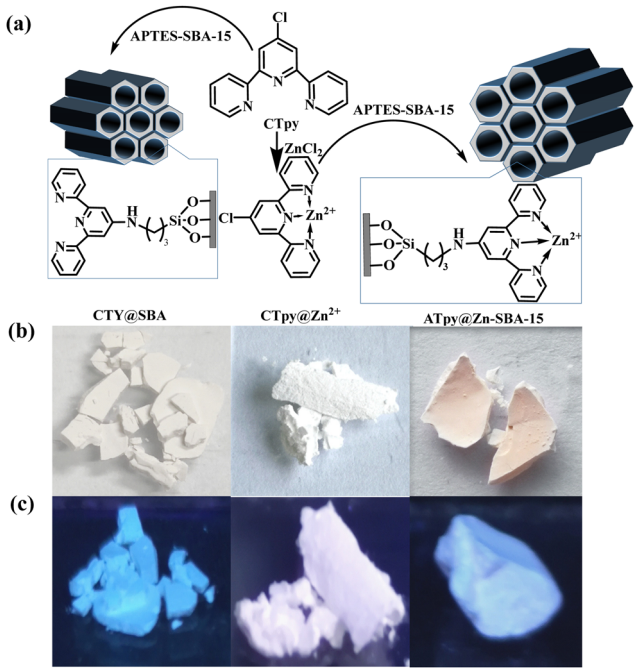

Scheme 1 (a) Synthetic process for CTY@SBA and ATpy@Zn-SBA-15, and optical photographs of ATpy-SBA-15, CTpy@Zn and ATpy@Zn-SBA-15 under (b) daylight) and (c) 365 nm UV light.

2.5. Fluorescence measurements

The ATpy@Zn-SBA-15 suspensions was prepared by adding 5 mg of ATpy@Zn-SBA-15 powder sample to 50 mL deionized water, ultrasonicating the suspension for 30 min to obtain uniform stock suspensions (0.1 g L^{-1}). The detection of SAs was performed as follows: 3 mL ATpy@Zn-SBA-15 stock suspensions were mixed with various amounts of SA solution (molecular structures of STZ, SCP, SMP, SMT and SMR are depicted in Fig. S1, ESI†) and diluted to 6 mL with 20 mM HEPES (pH = 7.0). The suspensions was mixed thoroughly and equilibrated at room temperature for 12 h. Afterward, the fluorescence spectra were recorded in the wavelength range of 315–560 nm, with the excitation wavelength of 298 nm. The ratio of the fluorescence intensity (I_0/I) was calculated as a response signal of ATpy@Zn-SBA-15 to SAs, where I_0 and I denote the fluorescence intensity of ATpy@Zn-SBA-15 in the absence and presence of SAs. Possible interferents such as representative metal ions; common anions; amino acids such as alanine (Ala), cysteine (Cys), and proline (Pro); and antibiotics such as amoxicillin (ACL), erythromycin (ERM), kanamycin sulfate (KNM) and gentamycin sulfate (GTM) were selected to test the SA selectivity of ATpy@Zn-SBA-15 under the same conditions.

The fluorescence-quenching efficiencies were calculated by using the formula E (%) = $(1 - I/I_0) \times 100\%$, where I_0 and I are the fluorescence intensities before and after the addition of each antibiotic, respectively. The limit of detection (LOD) was ascertained from the equation LOD = $3\sigma/s$, where σ is the standard deviation of 10 blank solutions, and s is the slope obtained from the linear calibration curve. The fluorescence-quenching efficiencies were further analyzed using the Stern–

Open Access Article. Published on 30 July 2022. Downloaded on 2/8/2026 2:57:13 PM.
This article is licensed under a Creative Commons Attribution-NonCommercial 3.0 Unported Licence.

Volmer equation, $(I_0/I - 1) = K_{sv}[Q]$, in which $[Q]$ is the molar concentration of the antibiotic, and K_{sv} is the quenching constant (M^{-1}).

2.6. Computational details for the energy of the lowest unoccupied molecular orbitals (LUMOs) and highest occupied molecular orbitals (HOMOs)

All calculations were carried out with the Gaussian 09 software package, and the geometric structures were optimized with the density functional theory (DFT) method using DFT/6-31G and 311G.

2.7. Reproducibility study

Approximately 40 mg of ATpy@Zn-SBA-15 was treated with STZ (200 μM) in 40 mL of water. After stirring at room temperature for 12 h, the fluorescent spectrum was recorded. Next, the mixture of ATpy@Zn-SBA-15 and STZ was centrifuged, sonicated, washed three times with MeOH, dried at 80 °C for 6 h and then reused for the determination of STZ. These processes were repeated three times.

2.8. Detection of STZ in real sample

Tap water and milk were selected as real samples for STZ detection. The milk sample was pretreated according to the reported methods.[37] Firstly, 10 mL of milk samples were treated with 1 mL of acetic acid (36 vol% ratio) and shaken for 1 min. The samples were diluted with deionized water (20 mL), shaken again, centrifuged (7000 rpm for 10 min) to remove the proteins and fat, filtered through diatomaceous earth and a 0.45 μm filter membrane, and then diluted with HEPES (20 mM, pH = 7.0) before analysis.

3. Results and discussion

3.1. Characterization of ATpy@Zn-SBA-15

As shown in Fig. 1A, the SXRD data displayed three well-resolved diffraction peaks that could be attributed to the (100), (110) and (200) reflections, demonstrating the existence of an ordered mesoporous structure after functionalizing SBA-15.[38] The TEM image (Fig. 1B) shows the highly ordered one-dimensional pore structure, which demonstrates that the ordered pore structure of mesoporous silica was unbroken after grafting CTpy@Zn^{2+}. The nitrogen adsorption–desorption data (Fig. 1C) revealed a type-IV isotherm, which is characteristic of mesoporous material with a uniform size distribution.[29] The BET surface area and total pore volume of ATpy@Zn-SBA-15 decreased to 332 $m^2\ g^{-1}$ and 0.96 $cm^3\ g^{-1}$ after CTpy@Zn^{2+} functionalization (Table S1, ESI†).

To further confirm the successful preparation of ATpy@Zn-SBA-15, the FT-IR spectra of CTpy@Zn^{2+}, SBA-15 and ATpy@Zn-SBA-15 were compared (Fig. 1D). The FT-IR spectra of CTpy@Zn^{2+} showed a peak at 3065 cm^{-1} corresponding to C–H stretching vibrations, and the peaks at 1595, 1479 and 1420 cm^{-1} correspond to C–C stretching vibrations of pyridyl group.[39] All three FT-IR spectra of SBA-15, APTES-SBA-15, and ATpy@Zn-SBA-15 revealed a broad O–H stretching band of the Si–OH groups at approximately 3423 cm^{-1}, a water peak caused by physical adsorption of materials at 1629 cm^{-1}, and characteristic Si–O–Si bands at 1078, 808, and 468 cm^{-1}, thereby confirming the existence of the SBA-15 silica framework. Compared with SBA-15, new peaks at 2960 and 2897 cm^{-1} appeared in APTES-SBA-15 and ATpy@Zn-SBA-15, which were attributed to the saturated hydrocarbon C–H group. Compared with APTES-SBA-15, the peak at 1542 cm^{-1} corresponding to N–H stretching vibration in ATpy@Zn-SBA-15 became weaker. These findings confirmed that ATpy@Zn-SBA-15 had been successfully prepared.

The loading of the organic motif on cubic silica surface was studied by TGA measurements. The TGA of ATpy@Zn-SBA-15 (Fig. S2, ESI†) displayed two weight loss regions between 30–170 and 170–800 °C. The former region showed a weight loss of water; the latter region revealed a weight loss of 11.31% in ATpy@Zn-SBA-15 owing to degradation of organic groups, and the calculated organic loading attachment was 0.32 mmol g^{-1}.

The validation of incorporating functional groups into the silica framework was further supported by solid-state MAS NMR. ^{13}C CP MAS NMR spectra of CTY@SBA (Fig. S3a, ESI†) showed three signals from the propyl carbon atom at 9.4, 26.4 and 43.9 ppm in the high-fat region, which was contributed by the APTES.[40] There were 15 signals from pyridine carbon atoms at 95–170 ppm. These signals were attributed to the anchoring of CTpy. Thus, the results of ^{13}C solid-state NMR successfully clarified the molecular composition of the functionalized organic moieties. Moreover, the ^{29}Si CP MAS NMR spectra (Fig. S3b, ESI†) showed two signals at −59.6 and −66.8 ppm, corresponding to the T^2 [$RSi(OSi)_2OH$] and T^3 [$RSi(OSi)_3$] resonances, respectively. Two other signals were detected, one at −100.6 ppm attributed to the Q^3 [$Si(OSi)_3OH$] resonance, and another at −108.7 ppm corresponding to the Q^4 [$Si(OSi)_4$] resonance. It should be noted that the appearance of T^2 and T^3 signals confirmed the existence of Si–C covalent bonds between organic groups and mesoporous silicas.[41,42] These results confirmed that terpyridine functional groups were successfully incorporated into the SBA-15 framework.

3.2. Optimization of detection conditions

As shown in the normalized fluorescence spectra (Fig. S4, ESI†), the emission band of ATpy@Zn-SBA-15 appeared at 429 nm, which was attributed to the aggregation of terpyridine. It had been reported that the working conditions not only affect the optical properties of the constructed sensor but also its sensing abilities toward analytes.[43] Therefore, the effects of pH and concentration on the fluorescence spectra of ATpy@Zn-SBA-15 were explored.

As shown in Fig. 2 and Fig. S5a, S6 (ESI†), the fluorescence emission intensity of ATpy@Zn-SBA-15 at 429 nm was higher than that of CTY@SBA in the pH range of 2.0–13.0, which could be due to the combination between CTY@SBA and Zn^{2+}, whereas ATpy@Zn-SBA-15 did not form in the strong acidic (pH < 2.0) and strong alkali media (pH > 13.0). Upon increasing pH from 2.0 to 4.0, the fluorescence intensity of ATpy@Zn-SBA-15

© 2022 The Author(s). Published by the Royal Society of Chemistry

Open Access Article. Published on 30 July 2022. Downloaded on 2/8/2026 2:57:13 PM.
This article is licensed under a Creative Commons Attribution-NonCommercial 3.0 Unported Licence.

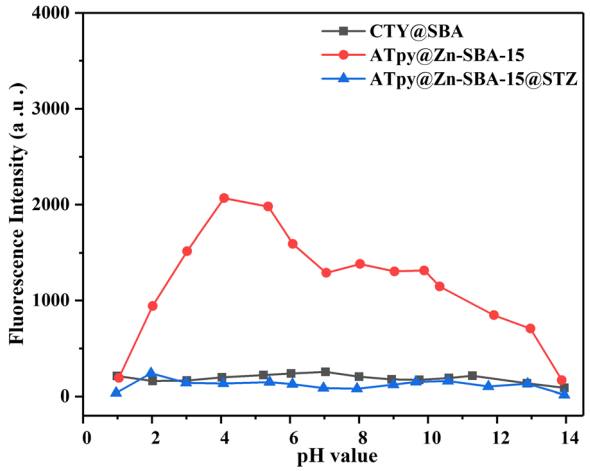

Fig. 2 Fluorescence intensity of CTY@SBA (0.05 g L^{-1}) and ATpy@Zn-SBA-15 (0.05 g L^{-1}) at 429 nm in the absence and presence of STZ (2.0×10^{-4} M) at different pH values.

at 429 nm increased gradually; however, the fluorescence intensity at 429 nm decreased when further increasing the pH, which was due to the formation of $Zn(OH)^{+}$, $Zn(OH)_2$, $Zn(OH)_3^{-}$ and $Zn(OH)_3^{2-}$ species[27] (Fig. S7a, ESI†), and the fluorescence emission of ATpy@Zn-SBA-15 at 429 nm was relatively stable in the pH range of 7.0–10.0.

The influence of concentration on the fluorescence of ATpy@Zn-SBA-15 was also studied. As the concentration of ATpy@Zn-SBA-15 increased from 0.05 to 1.00 g L^{-1}, the fluorescent intensity at 429 nm gradually increased, and the corresponding color of the suspensions of ATpy@Zn-SBA-15 changed from dark blue to bright blue (inset of Fig. S8a, ESI†). The fluorescent intensity at 429 nm *versus* the concentration of ATpy@Zn-SBA-15 displayed a linear relationship in the concentration range below 0.50 g L^{-1} (Fig. S8b, ESI†). Thus, unless otherwise stated, pH of 7.0 and concentration of 0.050 g L^{-1} were selected for the subsequent experiments.

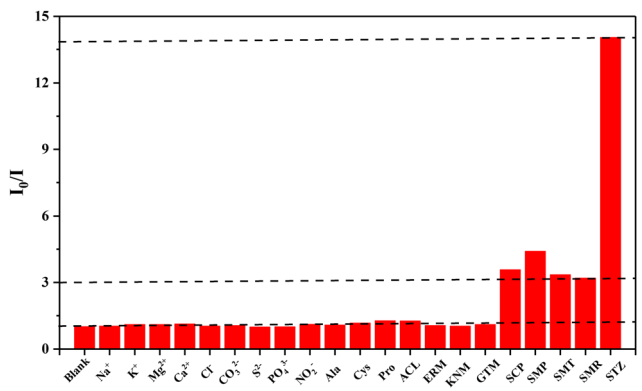

Fig. 3 Selectivity of SAs using ATpy@Zn-SBA-15 as a fluorescent sensor, corresponding normalized graph at λ_{em} = 429 nm, with metal cations, anions, amino acid and antibiotics (2.0×10^{-4} M) in HEPES buffer (20 mM, pH = 7.0; I_0 represents the original fluorescence intensity of ATpy@Zn-SBA-15, and I is the final fluorescence intensity after adding various analytes).

3.3. Selectivity

The fluorescence response of ATpy@Zn-SBA-15 in the presence of various competitive materials, such as metal ions, anions, amino acid and antibiotics, was investigated. As shown in Fig. 3 and Fig. S9 (ESI†), only SAs, including STZ, SCP, SMP, SMT and SMR, caused significant fluorescence quenching of ATpy@Zn-SBA-15; the changes (I_0/I) in fluorescence intensity of ATpy@Zn-SBA-15 at 429 nm were above 3-fold upon adding SAs; especially, the change was 14-fold for STZ, while small or subtle changes were observed upon adding the other investigated antibiotics, metal ions, common anions and amino acids. Thus, ATpy@Zn-SBA-15 could be applied as a fluorescent sensor for the detection of various SAs in water.

3.4. Sensitivity

As mentioned above, ATpy@Zn-SBA-15 showed observable fluorescence-quenching effects toward SAs in aqueous media. As shown in Fig. 4a, STZ induced considerable quenching effects on ATpy@Zn-SBA-15; as the concentration of STZ increased, the fluorescence intensity of ATpy@Zn-SBA-15 suspensions at 429 nm gradually decreased in the range of 0 to 2.0×10^{-4} M. ATpy@Zn-SBA-15 also exhibited significant quenching in the presence of the other SAs such as SMT, SCP, SMR and SMP (Fig. S10 and S11a, ESI†), with quenching efficiency varying from *ca.* 93.0% (STZ) to *ca.* 68.8% (SMR) (Fig. 5a).

As shown in the Stern–Volmer curves (Fig. 4b, 5b and Fig. S11b, ESI†), the fluorescence response of ATpy@Zn-SBA-15 at 429 nm was linear in the presence of STZ and SMP at the low concentration range of 0–60 μM. At higher concentrations, the curves diverged from linearity, and the slope increased gradually. This phenomenon was likely because of self-adsorption process.[44] To confirm the adsorption assumption, the adsorption capacity of ATpy@Zn-SBA-15 toward STZ was examined. STZ is nearly unadsorbed by ATpy@Zn-SBA-15, with the adsorption capacity of only 2 mg g^{-1} (Fig. S12, ESI†). Thus, the increased slope was not due to the self-adsorption process. The Stern–Volmer curves were nearly linear for the other SAs, such as SMT, SCP and SMR, in the entire range of concentration. From the linear fitting of the plots using the Stern–Volmer equation (inset of Fig. 4b and 5b), the K_{sv} values for STZ, SMT, SCP, SMR and SMP were found to be 2.65×10^4, 1.14×10^4, 1.12×10^4, 0.94×10^4 and 0.70×10^4 M^{-1}, respectively, indicating the excellent quenching ability of ATpy@Zn-SBA-15 toward STZ. According to the equation LOD = $3\sigma/s$, the LOD of the sensor for STZ, SMT, SCP, SMR and SMP was calculated to be 0.17, 0.63, 0.52, 0.57 and 0.54 μM, respectively (Table 1).

To evaluate the anti-interference properties of ATpy@Zn-SBA-15 as SA sensor, taking STZ as an example, the fluorescence response to STZ in the presence of other competitive material was tested. All the metal ions, common anions, amino acid and other antibiotics, caused no significant changes in sensing STZ (Fig. S13, ESI†). These results revealed that ATpy@Zn-SBA-15 was competently applicable for the detection of trace amounts of STZ in real samples.

There is no doubt that reusability of nanomaterials is an important element to be considered in the fluorescence

© 2022 The Author(s). Published by the Royal Society of Chemistry

Open Access Article. Published on 30 July 2022. Downloaded on 2/8/2026 2:57:13 PM.
This article is licensed under a Creative Commons Attribution-NonCommercial 3.0 Unported Licence.

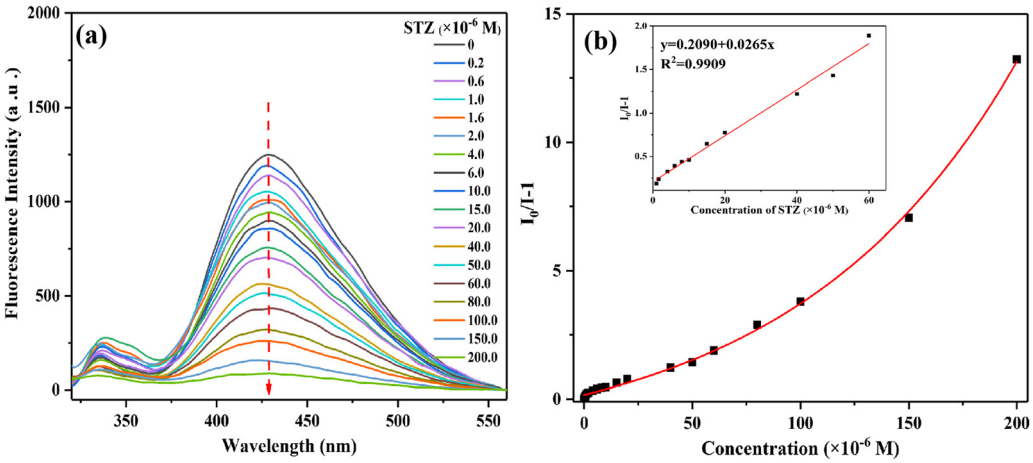

Fig. 4 (a) Fluorescence spectra of ATpy@Zn-SBA-15 (0.05 g L^{-1}) in the presence of different concentrations of STZ in aqueous solution (20 mM HEPES buffer, pH = 7.0); (b) Stern–Volmer plot for STZ. Inset: linear range of the Stern–Volmer plot (λ_{ex} = 298 nm, λ_{em} = 429 nm).

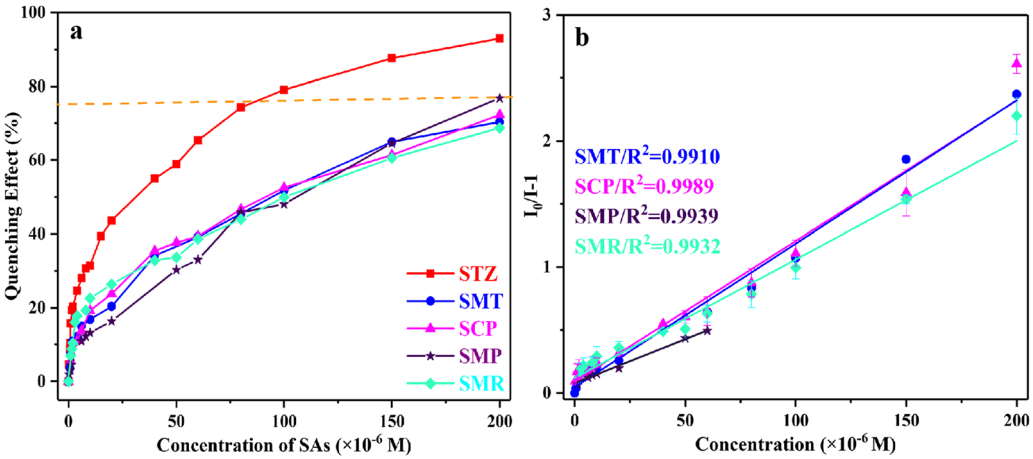

Fig. 5 (a) Concentration-dependent fluorescence-quenching scheme and (b) Stern–Volmer plots of various SAs.

Table 1 Detection parameters, K_{sv} and LOD of analytes

SAs	LOD/μM	K_{sv}/M^{-1}
STZ	0.17	2.65×10^4
SMT	0.63	1.14×10^4
SCP	0.52	1.12×10^4
SMR	0.57	0.94×10^4
SMP	0.54	0.70×10^4

detection process in order to obtain economic benefits. Therefore, regeneration experiments were conducted to assess the cyclicality of ATpy@Zn-SBA-15. As shown in Fig. S14 (ESI†), the fluorescence of the virgin aqueous suspension of ATpy@Zn-SBA-15 was quenched by treatment with 200 μM STZ solution and recovered after being washed with MeOH three times and dried at 80 °C. The renewed ATpy@Zn-SBA-15 can be re-applied for the detection of STZ, and the fluorescent process of turning off and on was realized by the resumed STZ detection and MeOH cleaning. In addition, the fluorescence sensing of ATpy@Zn-SBA-15 was repeated at least three times, with a recovery rate of at least 85%. Therefore, ATpy@Zn-SBA-15 showed a good recovery rate, indicating that this sensor has practical applications.

3.5. Possible sensing mechanism

As the above results demonstrated that ATpy@Zn-SBA-15 achieved high sensitivity for STZ among the SAs, the detection mechanism was investigated to understand the interaction between ATpy@Zn-SBA-15 and STZ. Considering that the pK_a values of STZ are 2.0 and 7.24, electrostatic repulsion forces might exist between the negatively charged surface of ATpy@Zn-SBA-15 and STZ^- at pH > 8.0. Thus, the effect of pH on the sensing capacity of ATpy@Zn-SBA-15 towards STZ was assessed (Fig. 2 and Fig. S5b, ESI†), in order to find out whether the electrostatic interaction contributed to the detection of ATpy@Zn-SBA-15 for STZ.[45] As obviously seen from Fig. S7 (ESI†), at pH = 7.0, the dominant species were STZ^0 and STZ^-, SMT^-, SCP^-, SMR^0 and SMR^-, SMP^0 and SMP^-. In the presence of STZ, the fluorescence intensity of ATpy@Zn-SBA-15 at

© 2022 The Author(s). Published by the Royal Society of Chemistry

Open Access Article. Published on 30 July 2022. Downloaded on 2/8/2026 2:57:13 PM.
This article is licensed under a Creative Commons Attribution-NonCommercial 3.0 Unported Licence.

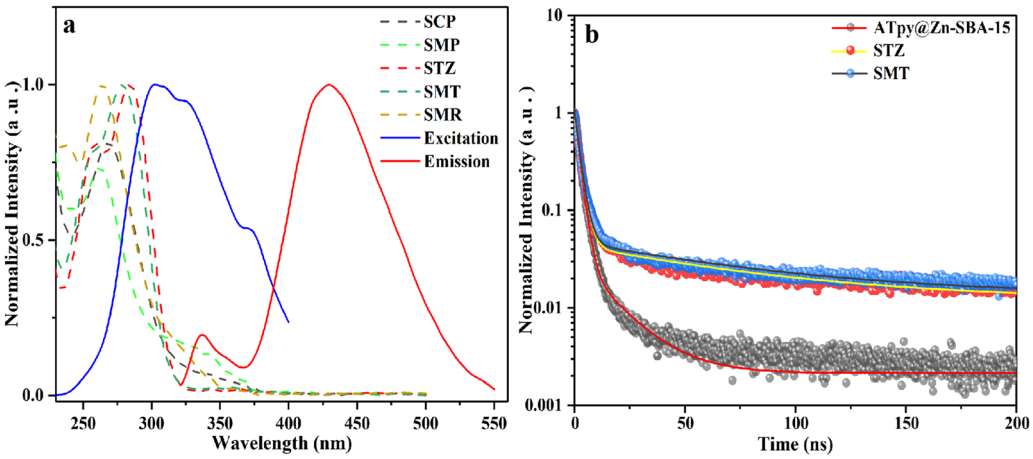

Fig. 6 (a) Normalized fluorescence spectrum of ATpy@Zn-SBA-15 and UV-Vis absorption spectra of SAs; (b) fluorescence decay curve of ATpy@Zn-SBA-15 in the absence and presence STZ and SMT.

429 nm was almost uninfluenced by the tested pH, indicating that STZ can be detected over a wide pH range of 2.0–13.0. Despite the electrostatic repulsion, the negative species of SMT and SCP also induced the fluorescence quenching of ATpy@Zn-SBA-15 at pH 7.0 (Fig. S10, ESI†). These results demonstrated that electrostatic interaction was not the main mechanism for SA sensing. Considering the stable pH range of ATpy@Zn-SBA-15 and the pK_a values of SAs (Table S3, ESI†), the pH for detecting SAs was selected at 7.0.

Fluorescence quenching can be caused by various mechanisms, such as the inner filter effect (IFE), fluorescence resonance energy transfer (FRET), electron transfer, *etc.* It was noted that there is negligible overlap between the absorption spectra of SAs and the emission spectra of ATpy@Zn-SBA-15 (Fig. 6a), excluding the possibility of FRET. In contrast, the absorption spectra of SAs overlapped with the excitation spectra of ATpy@Zn-SBA-15 (Fig. 6a); thus, the quenching mechanism could be IFE.

Fluorescence lifetime experiments were performed to verify the mechanism of fluorescence quenching induced by SAs (Fig. 6b and Table S2, ESI†). The fluorescence decay curve of ATpy@Zn-SBA-15 can be described by a double exponential function, giving the fast component T_1 of 1.97 ns and a slow component T_2 of 25.41 ns. According to the equation of $\tau_{average} = (B_1T_1 + B_2T_2)/(B_1 + B_2)$, the average fluorescence lifetime is 2.20 ns. After the addition of STZ and SMT, the average fluorescence lifetimes of ATpy@Zn-SBA-15 were 4.47 and 4.32 ns, respectively. Therefore, the changed fluorescence lifetime indicated that the fluorescence quenching could not be due to IFE. The increased fluorescence lifetime and the upward Stern–Volmer curve of ATpy@Zn-SBA-15 upon adding STZ indicated the existence of both dynamic and static quenching for STZ, and the increased fluorescence lifetime and the linear Stern–Volmer curve indicated dynamic quenching for SMT.[46]

To understand the role played by Zn^{2+}, the normalized fluorescence emission and excitation spectra of CTY@SBA and ATpy@Zn-SBA-15 were compared. CTY@SBA and ATpy@Zn-SBA-15 displayed an emission band at 429 nm with the excitation at 298 nm in aqueous media (Fig. S4, ESI†). In the presence of SAs, the fluorescence intensity of both CTY@SBA and ATpy@Zn-SBA-15 at 429 nm decreased; however, ATpy@Zn-SBA-15 appeared to be more sensitive to SAs than CTY@SBA when comparing the fluorescence changes ($I_0/I - 1$) (Fig. S15, ESI†). Moreover, it was noticed that the maximum excitation wavelength of ATpy@Zn-SBA-15 red shifted by 26 nm after adding STZ, which could be due to the formation of a complex between ATpy@Zn-SBA-15 and STZ, resulting in increased fluorescence lifetime.[47] By contrast, the maximum excitation spectra of CTY@SBA did not change in the presence of STZ, indicating that the improved SA sensitivity was due to the introduction of Zn^{2+} as the SA binding site.[30,48]

To further figure out the sensing mechanism, the energy levels of the HOMO and LUMO of SAs and the organic units on ATpy@Zn-SBA-15 were calculated (Table S3, ESI†). The LUMO energy level of the organic functions is higher than that of STZ, SMT and SCP, but lower than SMR and SMP, indicating that the electron transfer process is involved in the fluorescent quenching of ATpy@Zn-SBA-15 toward STZ, SMT and SCP,[38] and the quenching efficiency followed the order STZ (93.0%) > SCP (72.3%) ≈ SMT (70.3%) (Fig. 5). Moreover, the energy gap between the HOMO and LUMO in ATpy@Zn-SBA-15@STZ was lower than in both ATpy@Zn-SBA-15 and STZ due to the structure stabilization, which further confirmed the complex was formed between ATpy@Zn-SBA-15 and STZ (Fig. S16, ESI†). Therefore, the high sensitivity for STZ detection can be attributed to the combination between ATpy@Zn-SBA-15 and STZ through binding-site signaling subunit mechanism, which thus facilitates electron transfer from the organic functional group of ATpy@Zn-SBA-15 to STZ, resulting in efficient changes in fluorescence spectra.

3.6. Detection of STZ in real samples

The performance of ATpy@Zn-SBA-15 toward SAs has been compared with those nanomaterials based on different detection methods. As is apparent from Table S4 (ESI†), compared to most of the reported materials, ATpy@Zn-SBA-15 displayed several promising properties, such as fluorescence detection, which is convenient to operate and responds quickly; a wide

Open Access Article. Published on 30 July 2022. Downloaded on 2/8/2026 2:57:13 PM.
This article is licensed under a Creative Commons Attribution-NonCommercial 3.0 Unported Licence.

Table 2 Determination of STZ in real water samples (n = 3)

Sample	Spiked/μM	Found/μM	Recovery/%	RSD/%
Tap water	4.0	4.13 ± 0.26	103.2	2.49
	10.0	10.27 ± 0.14	102.7	0.56
	16.0	16.01 ± 0.38	100.1	0.97
Milk	4.0	4.16 ± 0.23	103.9	2.26
	10.0	10.07 ± 0.79	100.8	3.16
	16.0	16.10 ± 0.17	100.6	0.42

applicable pH range, which can be applied to detection in different environments; and comparable LOD.

The detection of STZ in real samples such as tap water and milk was carried out next, and a standard working plot was used to detect the concentration of STZ in the samples. As shown in Table 2, the concentration of STZ determined was nearly consistent with the amount added, and the quantitative recoveries of STZ were from 100.1 to 103.9%. These results indicated that the proposed strategy could detect trace amounts of STZ in tap water and milk simply and accurately.

4. Conclusion

In summary, an organic–metal functionalized mesoporous silica ATpy@Zn-SBA-15 was prepared and utilized as a sensitive fluorescent sensor for the detection of SAs in tap water and milk. Moreover, its good stability in water and MeOH also makes recyclability of the sensor materials a practical possibility. Compared with CTY@SBA, ATpy@Zn-SBA-15 exhibited exceptionally promoted sensing performance and low LOD for SAs due to the introduction of Zn^{2+} ions, which provided the SA coordination sites, enhancing the binding ability and recognition of ATpy@Zn-SBA-15 toward SAs. The fluorescence of ATpy@Zn-SBA-15 was quenched by SAs such as STZ *via* the binding-site signaling subunit mechanism, thus forming conjugates between ATpy@Zn-SBA-15 and STZ, enhancing the electron transfer from the organic functional groups of ATpy@Zn-SBA-15 to STZ. In view of its easy preparation, simple operation, good water dispersion stability, high sensitivity and low LOD, this approach could be feasible and effective for detecting trace amounts of other antibiotics by means of tuning the organic units and target-binding metal sites in the organic–metal functionalized mesoporous silica materials.

Conflicts of interest

There are no conflicts to declare.

Acknowledgements

This research was financially supported by the National Natural Science Foundation of China (No. 21966006).

References

1 P. Raja Lakshmi, P. Nanjan, S. Kannan and S. Shanmugaraju, Recent advances in luminescent metal–organic frameworks (LMOFs) based fluorescent sensors for antibiotics, *Coord. Chem. Rev.*, 2021, **435**, 213793.
2 I. M. Al-Riyami, M. Ahmed, A. Al-Busaidi and B. S. Choudri, Antibiotics in wastewaters: a review with focus on Oman, *Appl. Water Sci.*, 2018, **8**, 199.
3 R. Goswami, S. C. Mandal, N. Seal, B. Pathak and S. Neogi, Antibiotic–triggered reversible luminescence switching in amine–grafted mixed–linker MOF: exceptional turn–on and ultrafast nanomolar detection of sulfadiazine and adenosine monophosphate with molecular keypad lock functionality, *J. Mater. Chem. A*, 2019, **7**, 19471–19484.
4 M. S. Gaballah, J. Guo, H. Sun, D. Aboagye, M. Sobhi, A. Muhmood and R. Dong, A review targeting veterinary antibiotics removal from livestock manure management systems and future outlook, *Bioresour. Technol.*, 2021, **333**, 125069.
5 A. Moga, M. Vergara–Barberan, M. J. Lerma–Garcia, E. J. Carrasco–Correa, J. M. Herrero–Martinez and E. F. Simo–Alfonso, Determination of antibiotics in meat samples using analytical methodologies: A review, *Compr. Rev. Food Sci. Food Saf.*, 2021, **20**, 1681–1716.
6 L. Chen, Y. Liu, G. Cheng, Z. Fan, J. Yuan, S. He and G. Zhu, A novel fluorescent probe based on N, B, F co–doped carbon dots for highly selective and sensitive determination of sulfathiazole, *Sci. Total Environ.*, 2021, **759**, 143432.
7 T. Garoma, S. K. Umamaheshwar and A. Mumper, Removal of sulfadiazine, sulfamethizole, sulfamethoxazole, and sulfathiazole from aqueous solution by ozonation, *Chemosphere*, 2010, **79**, 814–820.
8 W. Zhang, J. Wan, W. Cui, L. Liu, L. Cao, G. Shen and S. Hu, Adsorption dynamics and mechanism of amoxicillin and sulfachlorpyridazine by ZrOx/porous carbon nanocomposites, *J. Taiwan Inst. Chem. Eng.*, 2019, **104**, 65–74.
9 A. P. S. Batista, A. Teixeira, W. J. Cooper and B. A. Cottrell, Correlating the chemical and spectroscopic characteristics of natural organic matter with the photodegradation of sulfamerazine, *Water Res.*, 2016, **93**, 20–29.
10 C. Alvarez–Esmoris, M. Conde–Cid, G. Ferreira–Coelho, M. J. Fernandez–Sanjurjo, A. Nunez–Delgado, E. Alvarez–Rodriguez and M. Arias–Estevez, Adsorption/desorption of sulfamethoxypyridazine and enrofloxacin in agricultural soils, *Sci. Total Environ.*, 2020, **706**, 136015.
11 J. Li, Y. Wang and X. Yu, Magnetic molecularly imprinted polymers: synthesis and applications in the selective extraction of antibiotics, *Front. Chem.*, 2021, **9**, 706311.
12 E. M. Golet, A. C. Alder, A. Hartmann, T. A. Ternes and W. Giger, Trace determination of fluoroquinolone antibacterial agents in urban wastewater by solid–phase extraction and liquid chromatography with fluorescence detection, *Anal. Chem.*, 2001, **73**, 3632–3638.
13 A. Gantverg, I. Shishani and M. Hoffman, Determination of chloramphenicol in animal tissues and urine, *Anal. Chim. Acta*, 2003, **483**, 125–135.
14 R. Wang, S. Li, D. Chen, Y. Zhao, Y. Wu and K. Qi, Selective extraction and enhanced–sensitivity detection of fluoroquinolones in swine body fluids by liquid chromatography–

© 2022 The Author(s). Published by the Royal Society of Chemistry

Open Access Article. Published on 30 July 2022. Downloaded on 2/8/2026 2:57:13 PM. This article is licensed under a Creative Commons Attribution-NonCommercial 3.0 Unported Licence.

high resolution mass spectrometry: application in long–term monitoring in livestock, *Food Chem.*, 2021, **341**, 128269.

15 M. Marimuthu, S. S. Arumugam, D. Sabarinathan, H. Li and Q. Chen, Metal organic framework based fluorescence sensor for detection of antibiotics, *Trends Food Sci. Technol.*, 2021, **116**, 1002–1028.

16 M. M. Sabzehmeidani and M. Kazemzad, Quantum dots based sensitive nanosensors for detection of antibiotics in natural products: A review, *Sci. Total Environ.*, 2021, **810**, 151997.

17 J. J. BelBruno, Molecularly imprinted polymers, *Chem. Rev.*, 2019, **119**, 94–119.

18 T. G. Kebede, S. Dube and M. M. Nindi, Application of mesoporous nanofibers as sorbent for removal of veterinary drugs from water systems, *Sci. Total Environ.*, 2020, **738**, 140282.

19 M. Gao, J. Zeng, K. Liang, D. Zhao and B. Kong, Interfacial assembly of mesoporous silica-based optical heterostructures for sensing applications, *Adv. Funct. Mater.*, 2020, **30**, 1906950.

20 X. D. Zhu, K. Zhang, Y. Wang, W. W. Long, R. J. Sa, T. F. Liu and J. Lu, Fluorescent metal–organic framework (MOF) as a highly sensitive and quickly responsive chemical sensor for the detection of antibiotics in simulated wastewater, *Inorg. Chem.*, 2018, **57**, 1060–1065.

21 H. Miao, Y. Wang and X. Yang, Carbon dots derived from tobacco for visually distinguishing and detecting three kinds of tetracyclines, *Nanoscale*, 2018, **10**, 8139–8145.

22 H. Goyal, S. Pachisia and R. Gupta, Systematic design of a low-molecular-weight gelator and its application in the sensing and retention of residual antibiotics, *Cryst. Growth Des.*, 2020, **20**, 6117–6128.

23 M. Fan, B. Sun, X. Li, Q. Pan, J. Sun, P. Ma and Z. Su, Highly fluorescent cadmium based metal-organic frameworks for rapid detection of antibiotic residues, Fe(3+) and Cr_2O_7(2-) ions, *Inorg Chem.*, 2021, **60**, 9148–9156.

24 Q. Q. Zhu, Q. S. Zhou, H. W. Zhang, W. W. Zhang, D. Q. Lu, M. T. Guo, Y. Yuan, F. Sun and H. He, Design and construction of a metal-organic framework as an efficient luminescent sensor for detecting antibiotics, *Inorg. Chem.*, 2020, **59**, 1323–1331.

25 Q. Gao, H. Zhu, W. J. Luo, S. Wang and C. G. Zhou, Preparation, characterization, and adsorption evaluation of chitosan–functionalized mesoporous composites, *Microporous Mesoporous Mater.*, 2014, **193**, 15–26.

26 L. Zhang and L. Chen, Fluorescence probe based on hybrid mesoporous silica/quantum dot/molecularly imprinted polymer for detection of tetracycline, *ACS Appl. Mater. Interfaces*, 2016, **8**, 16248.

27 Z. Dong, Z. Dong, P. Wang, X. Tian, H. Geng, R. Li and J. Ma, A fluorescent probe for zinc detection based on organically functionalized SBA–15, *Appl. Surf. Sci.*, 2010, **257**, 802–806.

28 L. Zhao, J. Li, D. Sui and Y. Wang, Highly selective fluorescence chemosensors based on functionalized SBA–15 for detection of Ag^+ in aqueous media, *Sens. Actuators, B*, 2017, **242**, 1043–1049.

29 J. Huang, J. Wang, D. Li, P. Chen and H. B. Liu, Terthiophene–functionalized mesoporous silica–based fluorescence sensor for the detection of trace methyl orange in aqueous media, *Mikrochim. Acta*, 2021, **188**, 410.

30 L. Wang, X. Han, T. Liang, X. Yan, X. Yang, Z. Pei, S. Tian, S. Wang, E. C. Lima and J. Rinklebe, Cosorption of Zn(II) and chlortetracycline onto montmorillonite: pH effects and molecular investigations, *J. Hazard. Mater.*, 2022, **424**, 127368.

31 D. H. Nakahata, R. E. F. de Paiva, W. R. Lustri, C. M. Ribeiro, F. R. Pavan, G. G. da Silva, A. Ruiz, J. E. de Carvalho and P. P. Corbi, Sulfonamide-containing copper(II) metallonucleases: Correlations with in vitro antimycobacterial and antiproliferative activities, *J. Inorg. Biochem.*, 2018, **187**, 85–96.

32 M. Ikram, J. Hassan, A. Raza, A. Haider, S. Naz, A. Ul-Hamid, J. Haider, I. Shahzadi, U. Qamar and S. Ali, Photocatalytic and bactericidal properties and molecular docking analysis of TiO_2 nanoparticles conjugated with Zr for environmental remediation, *RSC Adv.*, 2020, **10**, 30007–30024.

33 M. Ikram, M. I. Khan, A. Raza, M. Imran, A. Ul-Hamid and S. Ali, Outstanding performance of silver-decorated MoS_2 nanopetals used as nanocatalyst for synthetic dye degradation, *Phys. Rev. E*, 2020, **124**, 114246.

34 M. Ikram, R. Tabassum, U. Qumar, S. Ali, A. Ul-Hamid, A. Haider, A. Raza, M. Imran and S. Ali, Promising performance of chemically exfoliated Zr-doped MoS_2 nanosheets for catalytic and antibacterial applications, *RSC Adv.*, 2020, **10**, 20559–20571.

35 A. Raza, J. Z. Hassan, M. Ikram, S. Naz, A. Haider, A. Ul-Hamid, I. Shahzadi, J. Haider, S. Goumri-Said, M. B. Kanoun and S. Ali, Molecular docking and DFT analyses of magnetic cobalt doped MoS_2 and BN nanocomposites for catalytic and antimicrobial explorations, *Surf. Interfaces*, 2021, **27**, 101771.

36 J. Wang, X. Zhang, H. B. Liu, D. Zhang, H. Nong, P. Wu, P. Chen and D. Li, Aggregation induced emission active fluorescent sensor for the sensitive detection of Hg^{2+} based on organic–inorganic hybrid mesoporous material, *Spectrochim. Acta, Part A*, 2020, **227**, 117585.

37 X. Wu, H. Kuang, C. Hao, C. Xing, L. Wang and C. Xu, Paper supported immunosensor for detection of antibiotics, *Biosens. Bioelectron.*, 2012, **33**, 309–312.

38 H. B. Liu, Y. Liang, J. Liang, J. Wang, Q. Li, Y. Y. Liu, Q. Li, Y. Zhu and F. Dong, Pyrene derivative–functionalized mesoporous silica–Cu(2 +) hybrid ensemble for fluorescence ''turn–on'' detection of H_2S and logic gate application in aqueous media, *Anal. Bioanal. Chem.*, 2020, **412**, 905–913.

39 S. Y. Kang, H. Yin, K. Q. Zhang, X. Chen and K. Z. Wang, Chemosensing properties and logic gate behaviors of graphene quantum dot–appended terpyridine, *Mater. Sci. Eng. Carbon*, 2019, **99**, 657–668.

40 L. Mafra, T. Cendak, S. Schneider, P. V. Wiper, J. Pires, J. R. Gomes and M. L. Pinto, Structure of chemisorbed CO(2) species in amine-functionalized mesoporous silicas studied by solid-state NMR and computer modeling, *J. Am. Chem. Soc.*, 2017, **139**, 389–408.

Open Access Article. Published on 30 July 2022. Downloaded on 2/8/2026 2:57:13 PM.
This article is licensed under a Creative Commons Attribution-NonCommercial 3.0 Unported Licence.

41 J. Wang, W. Guo, J.-H. Bae, S.-H. Kim, J. Song and C.-S. Ha, Facile preparation of a multifunctional fluorescent nanosensor for chemical and biological applications, *J. Mater. Chem.*, 2012, **22**, 24681.
42 C. Lu, H. Yang, J. Wang, Q. Tan and L. Fu, Utilization of iron tailings to prepare high-surface area mesoporous silica materials, *Sci. Total Environ*, 2020, **736**, 139483.
43 S. Chatterjee and A. R. Paital, Functionalized cubic mesoporous silica as a non–chemodosimetric fluorescence probe and adsorbent for selective detection and removal of bisulfite anions along with toxic metal ions, *Adv. Funct. Mater.*, 2018, **28**, 1704726.
44 C. Ma, P. Li, L. Xia, F. Qu, R. M. Kong and Z. L. Song, A novel ratiometric fluorescence nanoprobe for sensitive determination of uric acid based on CD@ZIF–CuNC nanocomposites, *Mikrochim. Acta*, 2021, **188**, 259.
45 Z. Pei, S. Yang, L. Li, C. Li, S. Zhang, X. Q. Shan, B. Wen and B. Guo, Effects of copper and aluminum on the adsorption of sulfathiazole and tylosin on peat and soil, *Environ. Pollut.*, 2014, **184**, 579–585.
46 Z. Gao, M. Qiao, M. Tan, H. Peng and L. Ding, Surface functionalization of mesoporous silica nanoparticles with pyronine derivative for selective detection of hydrogen sulfide in aqueous solution, *Colloids Surf., A*, 2020, **586**, 124194.
47 J. Wang, Q. Ma, Y. Wang, Z. Li, Z. Li and Q. Yuan, New insights into the structure–performance relationships of mesoporous materials in analytical science, *Chem. Soc. Rev.*, 2018, **47**, 8766–8803.
48 Z. Zhang, H. Liu, L. Wu, H. Lan and J. Qu, Preparation of amino–Fe(III) functionalized mesoporous silica for synergistic adsorption of tetracycline and copper, *Chemosphere*, 2015, **138**, 625–632.

© 2022 The Author(s). Published by the Royal Society of Chemistry